Rigidifying Acyl Carrier Protein Domain in Iterative Type I PKS CalE8 Does Not Affect Its Function

Jackwee Lim,[†] Huihua Sun,[‡] Jing-Song Fan,[†] Iman Fahim Hameed,[†] Julien Lescar,[‡] Zhao-Xun Liang,[‡] and Daiwen Yang[†*]

[†]Department of Biological Sciences, National University of Singapore, Singapore; and [‡]School of Biological Sciences, Nanyang Technological University, Singapore

ABSTRACT Acyl carrier protein (ACP) domains shuttle acyl intermediates among the catalytic domains of multidomain type I fatty acid synthase and polyketide synthase (PKS) systems. It is believed that the unique function of ACPs is associated with their dynamic property, but it remains to be fully elucidated what type of protein dynamics is critical for the shuttling domain. Using NMR techniques, we found that the ACP domain of iterative type I PKS CalE8 from *Micromonospora echinospora* is highly dynamic on the millisecond-second timescale. Introduction of an interhelical disulfide linkage in the ACP domain suppresses the dynamics on the millisecond-second timescale and reduces the mobility on the picosecond-nanosecond timescale. We demonstrate that the full-length PKS is fully functional upon rigidification of the ACP domain, suggesting that although the flexibility of the disordered terminal linkers may be important for the function of the ACP domain, the internal dynamics of the helical regions is not critical for that function.

INTRODUCTION

Fatty acid synthases (FAS) and polyketide synthases (PKS) are divided into type I and type II systems (1,2). Type I systems are large, highly integrated modular proteins, and type II systems consist of small, discrete proteins. In general, a type I PKS module consists of ketosynthase (KS), acyltransferase (AT), acyl carrier protein (ACP), ketoreductase (KR), enoyl reductase (ER), and dehydratase (DH). These domains are involved in the following chain-elongation, modification, and termination steps during biosynthesis: AT loads the starter/intermediate and extender units (acetate, malonate, or propionate) to ACP and KS, respectively; KS catalyzes the Claisen condensation between the extender unit and the growing chain; and the keto-ester intermediate is then modified by the optional reductive components (ER, KR, and DH). During these processes, the growing polyketide intermediate is covalently tethered to the ACP domain via a thioester linkage and shuttled among the catalytic domains. The mature polyketide intermediate is usually off-loaded by a thioesterase to release the polyketide product. The number and combination of catalytic domains vary significantly among different PKSs. For the iterative type I PKS CalE8 containing six domains, ACP is located between AT and KR (Fig. 1 *a*).

ACPs play a central role in both FAS and PKS systems in the production of fatty acids and a wealth of secondary metabolites (1). ACPs are small (~9 kDa) monomeric domains and proteins in type I and II FAS/PKS systems, respectively (1,3). Although different ACPs have a low sequence identity, they adopt a canonical structure with three or four α-helices and contain a conserved serine residue located in the N-terminus of the second helix that serves to attach acyl intermediates (4). Also, they are highly conserved in the function of shuttling the intermediates among various partner enzymes or catalytic domains. Before an ACP can perform its function, it is first activated by ACP synthase or 4′-phosphopantetheinyl transferase (4′-PPTase), which attaches a phosphopantetheine group from coenzyme A (CoA) onto the conserved serine of ACP to tether the acyl intermediate as thiol ester. The activated ACP that carries the acyl intermediates interacts with different catalytic domains in the same protein for the type I system or with discrete enzymes for the type II system at different stages during biosynthesis (1,3).

The ability of ACPs to be recognized by a series of proteins and shuttling among different catalytic domains is believed to be associated with their dynamic property (4,5). Indeed, ACPs have been shown to be highly dynamic. The isolated type I ACP domain from rat is flexible in its N- and C-terminal regions, as well as in one of the loops (6). The ACP domain in the full-length yeast FAS has been proposed to function like a swinging arm, and its structure solved by x-ray crystallography has been suggested to represent a single conformation adopted by the FAS, indicating the flexibility of the ACP domain (7,8). For type II ACPs, dynamics on a wide range of timescales have been observed (9–12), but different ACPs display different dynamic features. Some type II ACPs, such as those from *Escherichia coli*, spinach, and parasite, exist in equilibrium between two states (12–14), but it is unclear whether the conformational exchange is relevant to ACP's function. Although many type II ACPs are folded at neutral pH, some ACPs reported from *Helicobacter pylori* (*hp*ACP) and *Vibrio harveyi* (*vh*ACP) are so mobile that they adopt a mainly disordered conformation in the absence of Mg^{2+} at neutral pH (15,16). However,

Submitted June 7, 2012, and accepted for publication August 2, 2012.

*Correspondence: dbsydw@nus.edu.sg

Editor: Patrick Loria.

0006-3495/12/09/1037/8 $2.00

http://dx.doi.org/10.1016/j.bpj.2012.08.006

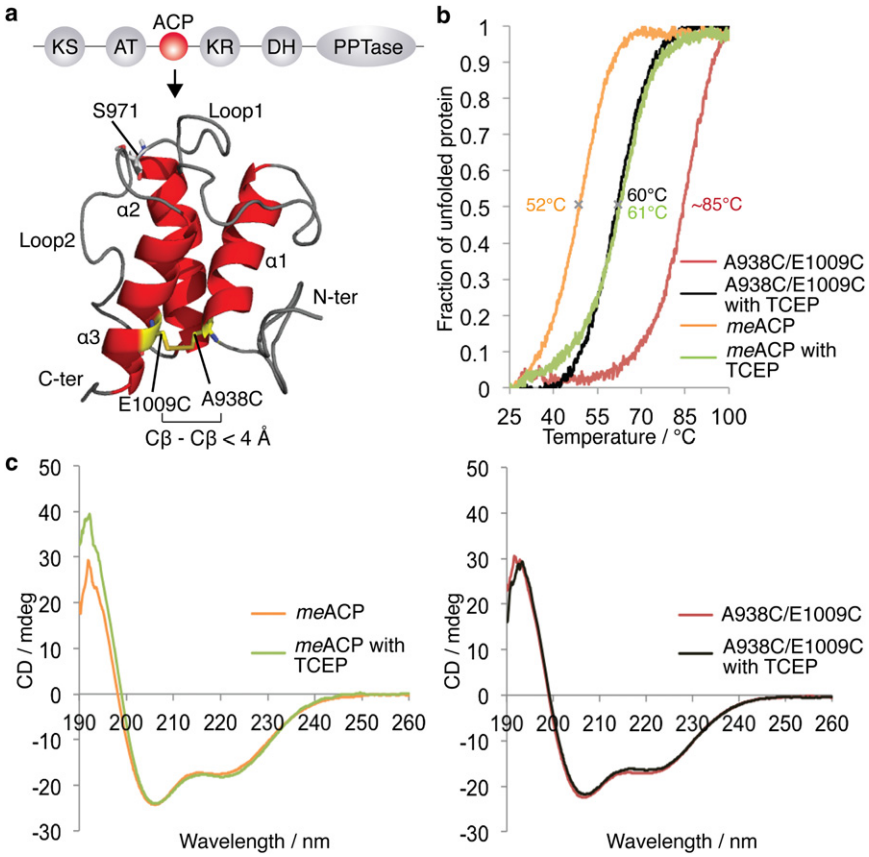

FIGURE 1 (*a*) Domain organization of CalE8 and ribbon structure of *me*ACP, with S971, A938C, and E1009C highlighted. (*b*) Thermal denaturation profiles of *me*ACP and its mutant monitored at 222 nm by CD. (*c*) CD profiles of *me*ACP and its mutant with and without 1.7 mM TCEP at 25°C.

such high mobility or disorder does not seem to be critical to ACP's function, because *vh*ACP and its cyclic form are equally functional even though the latter adopts a folded conformation (17). In addition, for the structurally and functionally similar peptidyl carrier protein (PCP) domain in the nonribosomal peptide synthetase (NRPS), apo-PCP and holo-PCP each exist in two slowly exchanging conformations and they share a common conformation (18). This conformational diversity has been shown to be important for the interactions of apo-PCP and holo-PCP with externally acting proteins such as 4′-PPTase and thioesterases. The conformational exchange also provides insight into the directed phosphopantetheine movement required for delivering substrates to upstream and downstream catalytic domains (18). However, the two observed holo-conformations could not explain how holo-PCP can recognize at least three partners (e.g., thioesterase, adenylation domain, and condensation domain) during biosynthesis.

Recently, we solved the solution structure of the ACP domain of iterative type I PKS CalE8 from *Micromonospora echinospora spp. calichensis* (*me*ACP), which is composed of a single module consisting of six catalytic domains for the synthesis of the putative precursor of the 10-member enediyne moiety (19). We showed that *me*ACP is highly dynamic on a timescale of seconds, although the helices are quite rigid on the picosecond-nanosecond timescale (19,20). Nevertheless, it is presently unclear whether the intrinsic flexibility is crucial for the shuttling of the ACP domain to perform its function within the compartmentalized chamber of the iterative PKS system. Here we demonstrate that we can dramatically reduce the internal dynamics of *me*ACP by introducing a disulfide linkage between helices 1 and 3, and that the dynamics of the structural region of the ACP domain on the picosecond-nanosecond and microsecond-second timescales is not critical for the function and activity of the iterative PKS CalE8.

MATERIALS AND METHODS

Samples preparation

We performed site-directed mutagenesis for *me*ACP and CalE8 using *Pfu* (Promega) and KOD Hot Start (Novagen) DNA polymerases, respectively, after Dpn1 digestion (Stratagene) and DNA gel electrophoresis purification. BL21 DH5α cell transformation was used to amplify the PCR product, which was later confirmed by sequencing. *me*ACP and CalE8 and their mutants were prepared according to previously described protocols (19,21,22). Coexpression of CalE8 and thioesterase CalE7 were performed as previously described (23).

Circular dichroism spectroscopy

Circular dichroism (CD) spectra were recorded on a Jasco J-810 spectropolarimeter equipped with a thermal controller. For disulfide bond reduction,

30 μM of protein was preincubated with 1.7 mM *tris*(2-carboxyethyl)phosphine (TCEP) for 10 min or 10 mM dithiothreitol (DTT) for 4 hr in 20 mM phosphate and 50 mM NaCl at pH 6.9, 25°C. Thermal unfolding was monitored at 222 nm in samples containing 30 μM protein, 20 mM phosphate, and 50 mM NaCl at pH 6.9.

NMR spectroscopy

All NMR experiments were performed on an 800 MHz NMR spectrometer equipped with a cryoprobe at 25°C, using ^{15}N-labeled samples containing 0.5 mM protein in 20 mM sodium phosphate buffer at pH 6.9, 50 mM NaCl. For hydrogen-deuterium (H-D) exchange experiments, the samples were lyophilized and then resuspended in D_2O. Three-dimensional (3D) ^{15}N-edited total correlation spectroscopy (TOCSY) and nuclear Overhauser spectroscopy (NOESY) experiments were performed with mixing times of 65 and 80 ms, respectively. Heteronuclear ^{15}N-{^{1}H} NOEs were measured using two spectra without and with proton saturation with a saturation delay of 4 s and recycle delay of 4 s by the inverse-detected 2D NMR method. Proton saturation was achieved by a train of 120° pulses spaced at 5 ms. Relaxation dispersion data were collected on both 500 and 800 MHz NMR spectrometers as described previously (24). In the presence of a series of Carr-Purcell-Meiboom-Gill (CPMG) fields (field strengths: 40, 80, 120, 160, 200, 240, 320, 400, 480, 560, 640, 720, 800 and 960 Hz), the apparent relaxation rates were measured using a constant time delay ($T_{CP} = 50$ ms) and interscan delay of 2 s. Dispersion curves were subsequently fitted with a two-site exchange model to extract kinetics parameters (25).

We measured the amide hydrogen exchange rates using a previously described pulse scheme (20) with an interscan delay of 2 s and 16 mixing times (20, 30, 40, 50, 60, 70, 80, 90, 100, 120, 140, 160, 190, 220, 260, and 300 ms). We recorded the reference spectrum used in the amide exchange measurement with a long interscan delay of 12 s. We measured the H-D exchange rates by monitoring the dependence of the ^{1}H-^{15}N HSQC peak intensities on the time after resuspending the lyophilized samples in D_2O.

CalE8 enzymatic assay

The enzymatic reactions for CalE8 were monitored with a UV-Vis spectrophotometer (22). A typical reaction contained 2.3 mg/ml CalE8 protein, 3.3 mg/ml CalE7, and 0.25 mM NADPH in a 100 mM HEPES buffer (pH 8.5) in a total volume of 200 μl. The absorption at 340 nm was autozeroed before addition of the substrate malonyl-CoA. Immediately after the addition of 1 mM malonyl-CoA, we recorded the progress of the reaction by following the absorption change at 340 nm. For the enzymatic reactions in the presence of TCEP, the reaction mixture was preincubated with 5 mM TCEP for 5–10 min before the addition of NADPH to initiate the reaction.

RESULTS AND DISCUSSION

Stabilization of *me*ACP by a disulfide linkage

On the basis of the *me*ACP structure (PDB ID: 2L9F), all cysteine candidates for potential disulfide linkages were identified and tested for protein expression and stability. In this study, we found that a disulfide linkage was successfully introduced by mutating A938 and E1009 into cysteines. Both A938 and E1009 are located far away from the conserved active serine residue (Ser-971) and their C_βs are in close proximity (<4 Å; Fig. 1 *a*). We expect that the cysteine mutant expressed in *E. coli* can form an intramolecular disulfide bond through thiol oxidation by O_2 dissolved in the buffer. It is noteworthy that the wild-type (WT) *me*ACP contains no cysteine residues. The formation of the expected disulfide bond was confirmed by mass spectrometry study of the mutant in the absence and presence of the reducing agent, DTT (see Fig. S1 in the Supporting Material). Moreover, thermal denaturation revealed that this mutant has remarkable thermostability relative to the WT *me*ACP (T_m was increased by 33°C from ~52°C to 85°C; Fig. 1 *b*). In the presence of TCEP (a more stable and effective reducing agent than DTT), the T_m of the mutant was nearly the same as that of *me*ACP, indicating that the significant increase in stability is indeed caused by the formation of a disulfide instead of the simple A938C/E1009C mutation effect. Interestingly, the T_m of the WT *me*ACP was ~10°C higher in the presence of TCEP than in the absence of TCEP, suggesting that TCEP can stabilize *me*ACP. In comparison, DTT has no stabilizing effect on *me*ACP (Fig. S2).

Structure of the stabilized *me*ACP mutant

CD spectroscopy shows that the A938C/E1009C mutation has little effect on the secondary structure profile of *me*ACP (Fig. 1 *c*). Using 3D ^{15}N-edited TOCSY and NOESY, and the previous assignments of WT *me*ACP, we assigned ^1H_N, ^{15}N, and aliphatic ^1H_C spins and obtained ^1H_N-^1H_C and ^1H_N-^1H_N NOEs for the *me*ACP mutant. The short- and medium-range NOE patterns (Fig. 2) and chemical shift index (Fig. S3) confirm that the secondary structure is barely influenced by the mutation, consistent with the CD results. Residues N995–A997 in front of the third helix may form a 3_{10} helix in the mutant based on the medium-range NOEs and chemical shift index. The long-range NOEs observed in the mutant sample are consistent with the 3D structure of the WT *me*ACP, demonstrating that the mutation does not change the tertiary structure significantly. However, the presence of a number of extra long-range NOEs in the mutant ($L939H_\beta$-$E1006H_N$ and $V942H_\gamma$-$L1008H_N$ (which are close to the disulfide linkage), $A947H_\beta$-$L952H_N$, $L964H_\delta$-$S970H_N$, $L977H_\delta$-$A950H_N$, $A982H_\beta$-$L987H_N$, $A982H_\beta$-$V990H_N$, $T998H_\alpha$-$E1003H_N$, $T1000H_\alpha$-$S961H_N$, and $V1001H_\gamma$-$R962H_N$) suggests that the mutant is more stable than the WT *me*ACP, consistent with the T_m result. Similarly to *me*ACP, the mutant gave rise to only one set of NMR signals, indicating that both the WT and mutant *me*ACP exist in a single major conformation.

Dynamics on the picosecond-nanosecond timescale

Heteronuclear ^{15}N-{^{1}H} NOE is very sensitive to the local mobility of an amide NH on the picosecond-nanosecond timescale. *me*ACP and its mutant show similar heteronuclear NOE profiles (Fig. 3).Similar to type I rat ACP (6), only the disordered terminal regions are very flexible. The average NOEs of the helices, loop 1, and loop 2 were respectively

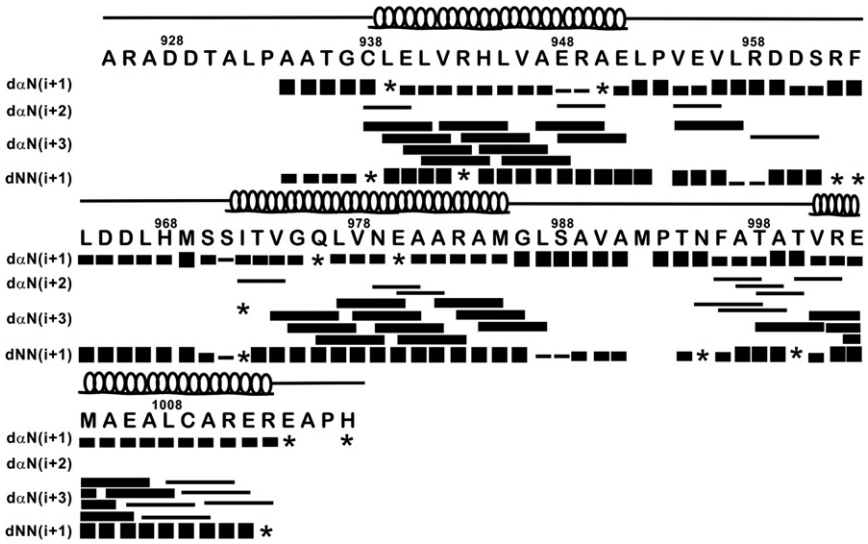

FIGURE 2 Sequential- and medium-range NOE patterns of the *me*ACP mutant. The NOE intensities are represented by the thickness of the solid bars. The secondary structure elements of the WT protein are indicated at the top of the sequence.

0.75, 0.73, and 0.64 for the WT *me*ACP, and 0.80, 0.79, and 0.68 for the mutant. The middle region of loop 2 had an average NOE value of 0.59 for both the WT and mutant *me*ACP. Similar to other globular proteins, the helical regions are quite rigid. Interestingly, loop 1 between helices 1 and 2 is as rigid as the helices, whereas the middle region of loop 2 is less rigid. Because the difference of the average NOEs (0.04) between the WT and mutant proteins is marginally larger than the average error (0.02), overall the mutant is slightly more rigid on the picosecond-nanosecond timescale.

Dynamics on microsecond-millisecond timescale

To investigate the dynamics on microsecond-millisecond timescale, we performed relaxation dispersion experiments.

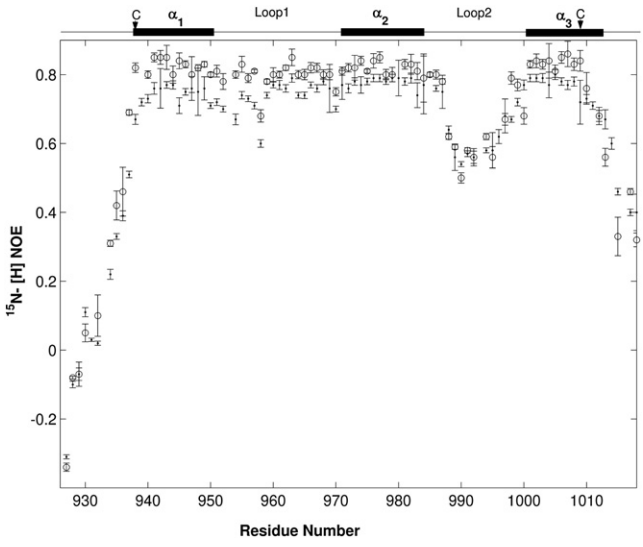

FIGURE 3 Comparison of ^{15}N-{^{1}H} NOEs for WT *me*ACP (•) and its mutant (○). The locations of two cysteine residues in the mutant are indicated by arrows on the secondary structure diagram.

The contribution of conformational exchange to ^{15}N transverse relaxation (R_{ex}) was estimated from relaxation rates (R_2^{eff}) measured at CPMG field strengths of 40 and 960 Hz on an 800 MHz NMR spectrometer, $R_{ex} = R_2^{eff}(\nu_{CP}, 40Hz) - R_2^{eff}(\nu_{CP}, 960Hz)$ (26). For *me*ACP (A925 – H1017), 74 out of 86 amides that were not overlapped and had good signal/noise (S/N) ratios displayed R_{ex}-values in the range of 1–11 s^{-1}, and 12 other residues that were mainly located in the disordered N-terminal region had $R_{ex} < 1\ s^{-1}$. To obtain reliable conformational exchange parameters, we employed only residues that had $R_{ex} > 2\ s^{-1}$ at both 500 and 800 MHz NMR to fit to a two-state theoretical model (25), which involved 58 amino acids distributing in three helices and two loops. The data were simultaneously fitted well to the model by a single set of exchange parameters (Fig. 4, *a–e*), indicating that *me*ACP likely exists in two states in solution. The exchange rate between the two states was found to be 301 ± 3 s^{-1}, and the populations of the major and minor states were 96.6% and 3.4%, respectively.

Due to the very low population of the minor form, the ^{15}N chemical shifts of the major state (δ_{ma}) were considered to be the same as those observed in the ^{1}H-^{15}N HSQC spectrum. The ^{15}N chemical shifts of the minor state (δ_{mi}) were calculated from δ_{ma} and the shift differences between the two states (Δ), which were extracted from the fitting of the relaxation dispersion data. Because the sign of Δ was not determined, we obtained two possible δ_{mi} values for each ^{15}N spin: $\delta_{ma} + \Delta$ and $\delta_{ma} - \Delta$. For a given amide ^{15}N, the δ_{mi} value close to the random coil ^{15}N chemical shift was considered to be the shift of the minor form. The random coil shifts used here were corrected for the sequence-dependent effects (27). The relatively good correlation between the δ_{mi} values and random coil shifts (Fig. 4 *f*) suggests that the invisible minor state likely exists in a partially disordered state. Also, it is possible that there

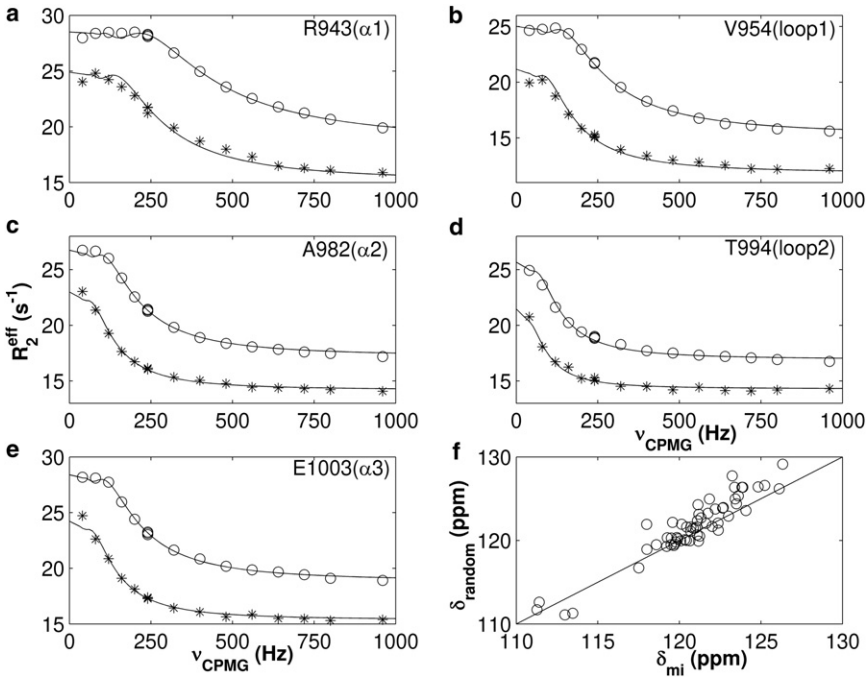

FIGURE 4 Representative relaxation dispersion profiles of *me*ACP (*a–e*) and comparison of experimental (δ_{mi}) and random coil (δ_{random}) ^{15}N chemical shifts of the invisible minor form (*f*). The experimental data recorded by 500 and 800 MHz NMR are indicated by ○ and *, respectively, and solid lines are fitting curves in panels *a–e*.

are two or more minor forms that exchange with one another as well as with the major form.

In contrast to the WT *me*ACP, the mutant displayed no relaxation dispersion for nearly all residues (Fig. S4, *a–e*). Only four residues (C938, R958, D960, and L967) had detectable R_{ex} (1–2 s^{-1}) on an 800 MHz NMR (Fig. S4 *f*). C938 is located at the beginning of helix 1, and R958, D960, and L967 are located in loop 1. The small R_{ex} likely resulted from local conformational exchange rather than global structural changes. The results demonstrate that the mutant is much more rigid than the WT protein on the microsecond-millisecond timescale.

Dynamics on the second timescale

Recently, we measured the amide hydrogen exchange rates (k_{ex}) of the WT *me*ACP and determined the protection (P) factors of amides (20). The average k_{ex} values for the residues in the three helices (excluding the three amides at the N-terminus of each helix, which are normally not involved in H-bonding), were ~0.4 s^{-1} at pH 6.9, and the average P factor was ~25. However, here we found that the k_{ex} values for most residues in the structural regions of the mutant were too small (<0.1 s^{-1}) to be detected by the amide hydrogen exchange experiment. To determine the dynamics of the mutant on the second timescale, we performed H-D exchange experiments. In contrast to the WT *me*ACP, in which amide protons were completely exchanged into deuterons within the NMR dead time (~3 min), the mutant was resistant to the H-D exchange, especially for the amides in the helices. The average k_{ex} value (at pH 6.9) and P factor for the helical residues were 6×10^{-4} s^{-1} and 2×10^4, respectively, which are changed by >600-fold compared with the result of the WT *me*ACP (Fig. 5). The results demonstrate that the mutant is much more rigid than the WT *me*ACP on the second timescale.

The rigidified *me*ACP domain retains its biological activity

Having established that the introduced disulfide linkage significantly reduces the internal flexibility of *me*ACP, we set out to test whether the reduced flexibility affects the function of the full-length PKS (CalE8). The A938C/E1009C mutation was introduced into the full-length CalE8 gene by site-directed mutagenesis. After overexpression in *E. coli*, the recombinant WT and mutant CalE8 were purified to homogeneity. The purified proteins exhibited bright yellow coloration with a broad absorbance around 400 nm (Fig. 6 *a*). It has been shown that the absorbance is attributed to the PKS-tethered polyene products synthesized in *E. coli* (21,22). This observation indicates that the mutant protein is enzymatically active and functional in *E. coli* cells. The result implies that the cysteine residues in the mutant CalE8 do not pair wrongly with the cysteine residues in other domains that contain 18 cysteine residues. Otherwise, the ACP domain would be permanently fixed at one or two domains through the incorrect interdomain disulfide linkages and would not be able to move to the catalytic centers in other domains. In addition, the two cysteine residues in the ACP domain of the mutant CalE8 should form an intradomain disulfide bond, as demonstrated in the isolated *me*ACP mutant (note that the two cysteine residues are in

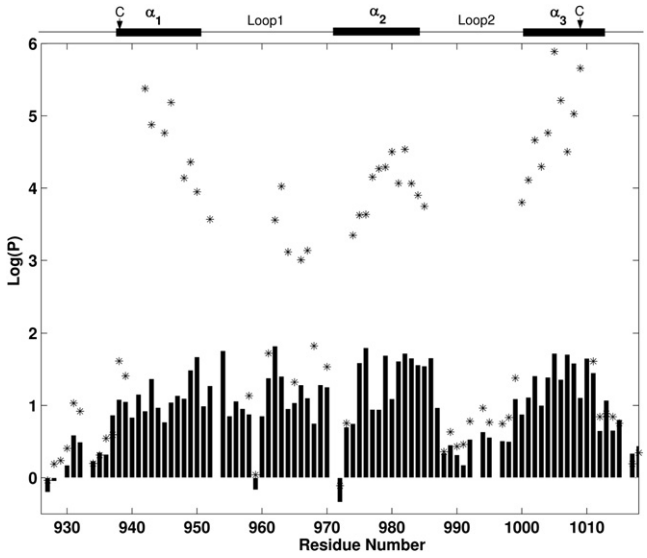

FIGURE 5 Comparison of P factors for WT (bar) and mutant (*) *me*ACP. P factors were calculated from amide hydrogen exchange rates (k_{ex}) and random coil exchange rates. For the WT *me*ACP, k_{ex} values were previously measured at pH 6.9 and 7.5 using an exchange spectroscopy (EXSY) scheme. For the mutant, k_{ex} values were obtained using either the EXSY scheme or the H-D exchange method. When $P < 100$ or $\log(P) < 2$, k_{ex} could be measured using the EXSY scheme. When $P > 1000$ or $\log(P) > 3$, k_{ex} could be measured using the H-D exchange scheme. When $100 < P < 1000$, k_{ex} could not be measured by these two methods. The locations of two cysteine residues in the mutant are indicated by arrows on the secondary structure diagram.

close proximity). To further evaluate the effect of the disulfide linkage on PKS activity, we performed in vitro assays. The WT and mutant CalE8 were coexpressed with thioesterase CalE7 to remove the covalently linked PKS products from the CalE8 (23). The proteins were purified without adding reducing agent in the lysis and purification buffer, and further exposed to air for several hours to ensure the formation of the disulfide linkage. The product-free PKS proteins were assayed for their enzymatic activity by absorption spectroscopy. By monitoring the consumption

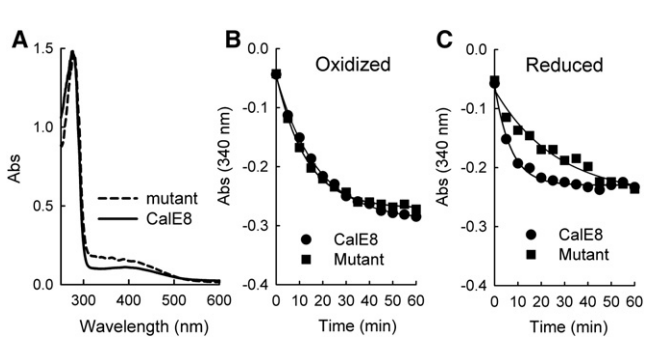

FIGURE 6 Enzymatic activity of CalE8 and the double mutant. (*A*) Absorption spectra of the WT and mutant CalE8 expressed from *E. coli*. (*B* and *C*) Comparison of the enzymatic activity of CalE8 and the double mutant under (*B*) oxidizing and (*C*) reducing conditions.

of the substrate NADPH, we found that the WT and mutant CalE8 exhibited nearly identical enzymatic efficiency (Fig. 6 *b*). After the disulfide bond in PKS CalE8 was reduced by preincubating the enzymes with TCEP, the mutant CalE8 exhibited slightly lower enzymatic efficiency (Fig. 6 *c*). Together, these results suggest that the reduced internal dynamics in the ACP domain has little effect on the overall activity of the iterative PKS CalE8.

Are the observed ACP dynamics critical for ACP function?

Different ACPs with low sequence identity adopt a very similar overall structure (4) but display very different dynamics over a wide range of timescales. The type I PKS *me*ACP shown here is quite rigid on the picosecond-nanosecond timescale, except for the middle region of loop 2 and two terminal regions. The entire WT *me*ACP is very dynamic on the millisecond-second timescale and it may exist in two conformations (one major and one minor form) that undergo intermediate exchange in the NMR time regime. The type I FAS apo-ACP from rat is mobile on the picosecond-nanosecond timescale only for the two terminal regions and the middle region of loop 1 instead of loop 2 (6). The rat apo-ACP domain exists in a single folded form and is quite rigid on the microsecond-millisecond timescale, except for Asp-2150 adjacent to Ser-2151, which is the phosphopantetheine attachment site (6). This is dramatically different from the type I *me*ACP.

For type II oxytetracycline apo-ACP, loop 1 is flexible on the picosecond-nanosecond timescale and helix 2 (the proposed recognition region) is mobile on the microsecond-millisecond timescale (9). For type II frenolicin holo-ACP, loop 1 is mobile on the picosecond-nanosecond timescale but the short helix 3′ is mobile on the microsecond-millisecond timescale (10). Helix 3′ is absent in most of the frenolicin ACP NMR structures and completely absent in *me*ACP. Type II spinach FAS apo- and holo-ACPs (28,29) each exist in two forms that are in slow exchange, and one of the forms is largely unfolded. Type II *E. coli* ACP (*ec*ACP) also exists in two forms, but the two forms are in fast exchange (12,13). Although two conformational states were observed for the holo-ACP from Plasmodium *falciparum* (14) and holo-ACP from *Mycobacterium tuberculosis* (30), they are caused by the reorientation of the phosphopantetheine prosthetic group rather than the intrinsic dynamics of the proteins. Most amide protons located in the helices of *ec*ACP are protected from H-D exchange (P factor > 1000) (11), implying rigidity on the second timescale, whereas the amide protons in *me*ACP are poorly protected (P factor < 80) (20). Type II *vh*ACP is unfolded in the absence of divalent ions, but it becomes folded in the presence of Mg^{2+} or Ca^{2+} (16,31). Because the basal level of Mg^{2+} is 1–2 mM in bacteria (32), *vh*ACP should function in a folded state in vivo.

A recent study on type II spinach ACP showed that the protein dynamics are influenced by the length of the fatty acids that are attached to the protein (33). Actually, this is reasonable because the fatty acid chain is sequestered by the hydrophobic cavity in type II ACPs (28). In contrast to type II ACPs, the type I ACP domains do not interact with either the fatty acid chain or the phosphopantetheine prosthetic group (6,19). Thus, we expect that the acylation of type I ACPs does not affect the dynamics of the protein. Because all ACPs perform the same function, i.e., shuttling acyl intermediates to a series of partners during biosynthesis, the dramatically varied dynamics among different ACPs should not correlate with their function. Our mutant and WT CalE8 enzymes have the same biological activities, demonstrating that the intrinsic dynamics of the structural region (A938-R1013 for *me*ACP) of type I ACP on the picosecond-nanosecond, microsecond-millisecond, and second timescales are not critical for its function.

For the *me*ACP construct used here (A925 – H1017), the 14 N-terminal residues and four C-terminal residues are unstructured and flexible (Figs. 2 and 3). In CalE8, ~50 residues preceding the first helix and ~40 residues following the last helix of *me*ACP domain were predicted to be unstructured (Fig. S5). Very likely, these residues form two long flexible linkers that permit *me*ACP to shuttle among different catalytic domains in a swinging manner. Recently, a swinging model was proposed for the delivery of substrates by ACP to different catalytic domains in the yeast FAS system, where the N-terminal region (136 residues) of the ACP domain is flexible and its C-terminus is connected to the center of the FAS particle through a flexible hinge with ~60 residues (7).

CONCLUSION

In summary, we found that the ACP domain of the iterative type I PKS CalE8 is highly dynamic on the millisecond-second timescale in the region that encompasses the three helices, loop 2, and loop 1 that is near the active serine. The mutant with a disulfide linkage between helices 1 and 3 is more rigid on the same timescale and much more stable against thermal denaturation, whereas its flexibility is only slightly lower than that of the WT *me*ACP on the picosecond-nanosecond timescale. Despite the significant reduction in the flexibility of the ACP domain, the full-length CalE8 mutant is fully active and capable of synthesizing the PKS products at the same rate as the WT enzyme. Hence, the internal dynamics of the structural region of *me*ACP does not seem to be critical for the function of the iterative PKS CalE8 and probably many other iterative PKSs. Nonetheless, the disordered terminal regions are flexible and may be important for the function of type I ACPs, which are connected to the two flanking catalytic domains. In addition, we cannot exclude the possibility that ACP's dynamics on the nanosecond-microsecond timescale, which was undetectable in our NMR experiments, is necessary for function.

SUPPORTING MATERIAL

Five figures are available at http://www.biophysj.org/biophysj/supplemental/S0006-3495(12)00866-1.

The authors thank Ms. Shujing Wang for help with the H-D exchange experiment. We are grateful for the use of the mass spectrometer at the Protein and Proteomics Center, National University of Singapore.

This research was supported by grants from the Ministry of Education, Singapore, to D.Y. (R154000453112) and Z.X.L.

REFERENCES

1. Mercer, A. C., and M. D. Burkart. 2007. The ubiquitous carrier protein—a window to metabolite biosynthesis. *Nat. Prod. Rep.* 24: 750–773.
2. Piel, J. 2010. Biosynthesis of polyketides by trans-AT polyketide synthases. *Nat. Prod. Rep.* 27:996–1047.
3. Lai, J. R., A. Koglin, and C. T. Walsh. 2006. Carrier protein structure and recognition in polyketide and nonribosomal peptide biosynthesis. *Biochemistry.* 45:14869–14879.
4. Byers, D. M., and H. S. Gong. 2007. Acyl carrier protein: structure-function relationships in a conserved multifunctional protein family. *Biochem. Cell Biol.* 85:649–662.
5. Chan, D. I., and H. J. Vogel. 2010. Current understanding of fatty acid biosynthesis and the acyl carrier protein. *Biochem. J.* 430:1–19.
6. Płoskoń, E., C. J. Arthur, …, M. P. Crump. 2008. A mammalian type I fatty acid synthase acyl carrier protein domain does not sequester acyl chains. *J. Biol. Chem.* 283:518–528.
7. Lomakin, I. B., Y. Xiong, and T. A. Steitz. 2007. The crystal structure of yeast fatty acid synthase, a cellular machine with eight active sites working together. *Cell.* 129:319–332.
8. Leibundgut, M., S. Jenni, …, N. Ban. 2007. Structural basis for substrate delivery by acyl carrier protein in the yeast fatty acid synthase. *Science.* 316:288–290.
9. Findlow, S. C., C. Winsor, …, M. P. Crump. 2003. Solution structure and dynamics of oxytetracycline polyketide synthase acyl carrier protein from *Streptomyces rimosus*. *Biochemistry.* 42:8423–8433.
10. Li, Q., C. Khosla, …, C. W. Liu. 2003. Solution structure and backbone dynamics of the holo form of the frenolicin acyl carrier protein. *Biochemistry.* 42:4648–4657.
11. Andrec, M., R. B. Hill, and J. H. Prestegard. 1995. Amide exchange rates in *Escherichia coli* acyl carrier protein: correlation with protein structure and dynamics. *Protein Sci.* 4:983–993.
12. Kim, Y., and J. H. Prestegard. 1989. A dynamic model for the structure of acyl carrier protein in solution. *Biochemistry.* 28:8792–8797.
13. Kim, Y., J. B. Ohlrogge, and J. H. Prestegard. 1990. Motional effects on NMR structural data. Comparison of spinach and *Escherichia coli* acyl carrier proteins. *Biochem. Pharmacol.* 40:7–13.
14. Sharma, A. K., S. K. Sharma, …, S. P. Sarma. 2006. Solution structures of conformationally equilibrium forms of holo-acyl carrier protein (PfACP) from *Plasmodium falciparum* provides insight into the mechanism of activation of ACPs. *Biochemistry.* 45:6904–6916.
15. Park, S. J., J. S. Kim, …, B. J. Lee. 2004. pH-induced conformational transition of *H. pylori* acyl carrier protein: insight into the unfolding of local structure. *J. Biochem.* 135:337–346.
16. Flaman, A. S., J. M. Chen, …, D. M. Byers. 2001. Site-directed mutagenesis of acyl carrier protein (ACP) reveals amino acid residues involved in ACP structure and acyl-ACP synthetase activity. *J. Biol. Chem.* 276:35934–35939.

17. Volkmann, G., P. W. Murphy, …, D. M. Byers. 2010. Intein-mediated cyclization of bacterial acyl carrier protein stabilizes its folded conformation but does not abolish function. *J. Biol. Chem.* 285:8605–8614.

18. Koglin, A., M. R. Mofid, …, V. Dötsch. 2006. Conformational switches modulate protein interactions in peptide antibiotic synthetases. *Science.* 312:273–276.

19. Lim, J., R. Kong, …, D. Yang. 2011. Solution structures of the acyl carrier protein domain from the highly reducing type I iterative polyketide synthase CalE8. *PLoS ONE.* 6:e20549.

20. Fan, J. S., J. Lim, …, D. Yang. 2011. Measurement of amide hydrogen exchange rates with the use of radiation damping. *J. Biomol. NMR.* 51:151–162.

21. Kong, R., L. P. Goh, …, Z. X. Liang. 2008. Characterization of a carbonyl-conjugated polyene precursor in 10-membered enediyne biosynthesis. *J. Am. Chem. Soc.* 130:8142–8143.

22. Sun, H., R. Kong, …, Z. X. Liang. 2009. Products of the iterative polyketide synthases in 9- and 10-membered enediyne biosynthesis. *Chem. Commun. (Camb.).* 47:7399–7401.

23. Kotaka, M., R. Kong, …, Z. X. Liang. 2009. Structure and catalytic mechanism of the thioesterase CalE7 in enediyne biosynthesis. *J. Biol. Chem.* 284:15739–15749.

24. Long, D., M. Liu, and D. Yang. 2008. Accurately probing slow motions on millisecond timescales with a robust NMR relaxation experiment. *J. Am. Chem. Soc.* 130:2432–2433.

25. Tollinger, M., N. R. Skrynnikov, …, L. E. Kay. 2001. Slow dynamics in folded and unfolded states of an SH3 domain. *J. Am. Chem. Soc.* 123:11341–11352.

26. Long, D., and D. Yang. 2010. Millisecond timescale dynamics of human liver fatty acid binding protein: testing of its relevance to the ligand entry process. *Biophys. J.* 98:3054–3061.

27. Schwarzinger, S., G. J. Kroon, …, H. J. Dyson. 2001. Sequence-dependent correction of random coil NMR chemical shifts. *J. Am. Chem. Soc.* 123:2970–2978.

28. Zornetzer, G. A., B. G. Fox, and J. L. Markley. 2006. Solution structures of spinach acyl carrier protein with decanoate and stearate. *Biochemistry.* 45:5217–5227.

29. Kim, Y. M., and J. H. Prestegard. 1990. Demonstration of a conformational equilibrium in acyl carrier protein from spinach using rotating frame nuclear magnetic resonance spectroscopy. *J. Am. Chem. Soc.* 112:3707–3709.

30. Wong, H. C., G. H. Liu, …, J. Zheng. 2002. The solution structure of acyl carrier protein from Mycobacterium tuberculosis. *J. Biol. Chem.* 277:15874–15880.

31. Chan, D. I., B. C. H. Chu, …, H. J. Vogel. 2010. NMR solution structure and biophysical characterization of *Vibrio harveyi* acyl carrier protein A75H: effects of divalent metal ions. *J. Biol. Chem.* 285: 30558–30566.

32. Alatossava, T., H. Jütte, …, E. Kellenberger. 1985. Manipulation of intracellular magnesium content in polymyxin B nonapeptide-sensitized *Escherichia coli* by ionophore A23187. *J. Bacteriol.* 162: 413–419.

33. Zornetzer, G. A., J. Tanem, …, J. L. Markley. 2010. The length of the bound fatty acid influences the dynamics of the acyl carrier protein and the stability of the thioester bond. *Biochemistry.* 49:470–477.